(d) Answer (a), (b) and (c) for an Al–2 wt% Cu alloy solidified under the same conditions.

4.16 (a) Using Equation 4.33 and the data in problem 4.15 plot the variation of copper concentration along a unidirectionally solidified bar of an Al–2 wt% Cu alloy assuming no diffusion in the solid and perfect mixing in the liquid.

(b) What fraction of the bar will solidify to a eutectic structure?

(c) How much eutectic would form in an Al–0.5 wt% Cu alloy solidified under the same conditions?

4.17 Explain the experimental observation that in the presence of a convection current cells grow upstream.

4.18 Sketch a possible solidification-front structure for the solidification of an Fe–0.25 wt% C alloy in a shallow temperature gradient. Consider the temperature range 1440–1540 °C. Assume very rapid diffusion of carbon in δ–Fe.

4.19 Show that the condition $\lambda = 2\lambda^*$ gives (i) the maximum eutectic growth rate for a given undercooling, and (ii) a minimum undercooling for a given growth rate (Equation 4.43).

4.20 Calculate the depression of the eutectic temperature for a lamellar eutectic with $\lambda = 0.2$ μm and $\lambda = 1.0$ μm, if $\gamma_{\alpha\beta} = 400$ mJ m^{-2}, $\Delta H/V_m = 800 \times 10^6$ J m^{-3}, $T_E = 1000$ K.

4.21 If it is assumed that the choice of a rod or lamellar eutectic is governed by the minimization of the total α/β interfacial energy it can be shown that for a given λ there is a critical volume fraction of the β phase (f_c) below which β should be rod like, and above which it should be lamellar. Assuming the rods are hexagonally arranged and that $\gamma_{\alpha\beta}$ is isotropic, calculate the value of f_c.

4.22 Compare the processes of ingot casting and weld solidification, and show they are in many ways quite different solidification processes. How would you compare continuous casting in this respect?

4.23 What is the influence of welding speed on the solidification structure of welds? How is welding speed likely to affect segregation problems?

5
Diffusional Transformations in Solids

The majority of phase transformations that occur in the solid state take place by thermally activated atomic movements. The transformations that will be dealt with in this chapter are those that are induced by a change of temperature of an alloy that has a fixed bulk composition. Usually we will be concerned with the transformations caused by a temperature change from a single-phase region of a (binary) phase diagram to a region where one or more other phases are stable. The different types of phase transformations that are possible can be roughly divided into the following groups: (a) precipitation reactions, (b) eutectoid transformations, (c) ordering reactions, (d) massive transformations, and (e) polymorphic changes. Figure 5.1 shows several different types of binary phase diagrams that are representative of these transformations.

Precipitation transformations can be expressed in reaction terms as follows

$$\alpha' \rightarrow \alpha + \beta \tag{5.1}$$

where α′ is a metastable *supersaturated solid solution*, β is a stable or metastable precipitate, and α is a more stable solid solution with the same crystal structure as α′, but with a composition closer to equilibrium, see Fig. 5.1a.

Eutectoid transformations involve the replacement of a metastable phase (γ) by a more stable mixture of two other phases (α + β) and can be expressed as

$$\gamma \rightarrow \alpha + \beta \tag{5.2}$$

This reaction is characteristic of phase diagrams such as that shown in Fig. 5.1b.

Both precipitation and eutectoid transformations involve the formation of phases with a different composition to the matrix and therefore long-range diffusion is required. The remaining reaction types can, however, proceed without any composition change or long-range diffusion. Figure 5.1c shows phase diagrams where *ordering reactions* can occur. In this case the reaction can be simply written

$$\alpha(\text{disordered}) \rightarrow \alpha'(\text{ordered}) \tag{5.3}$$

In a *massive* transformation the original phase decomposes into one or more new phases which have the same composition as the parent phase, but different crystal structures. Figure 5.1d illustrates two simple examples of the type

$$\beta \rightarrow \alpha \tag{5.4}$$

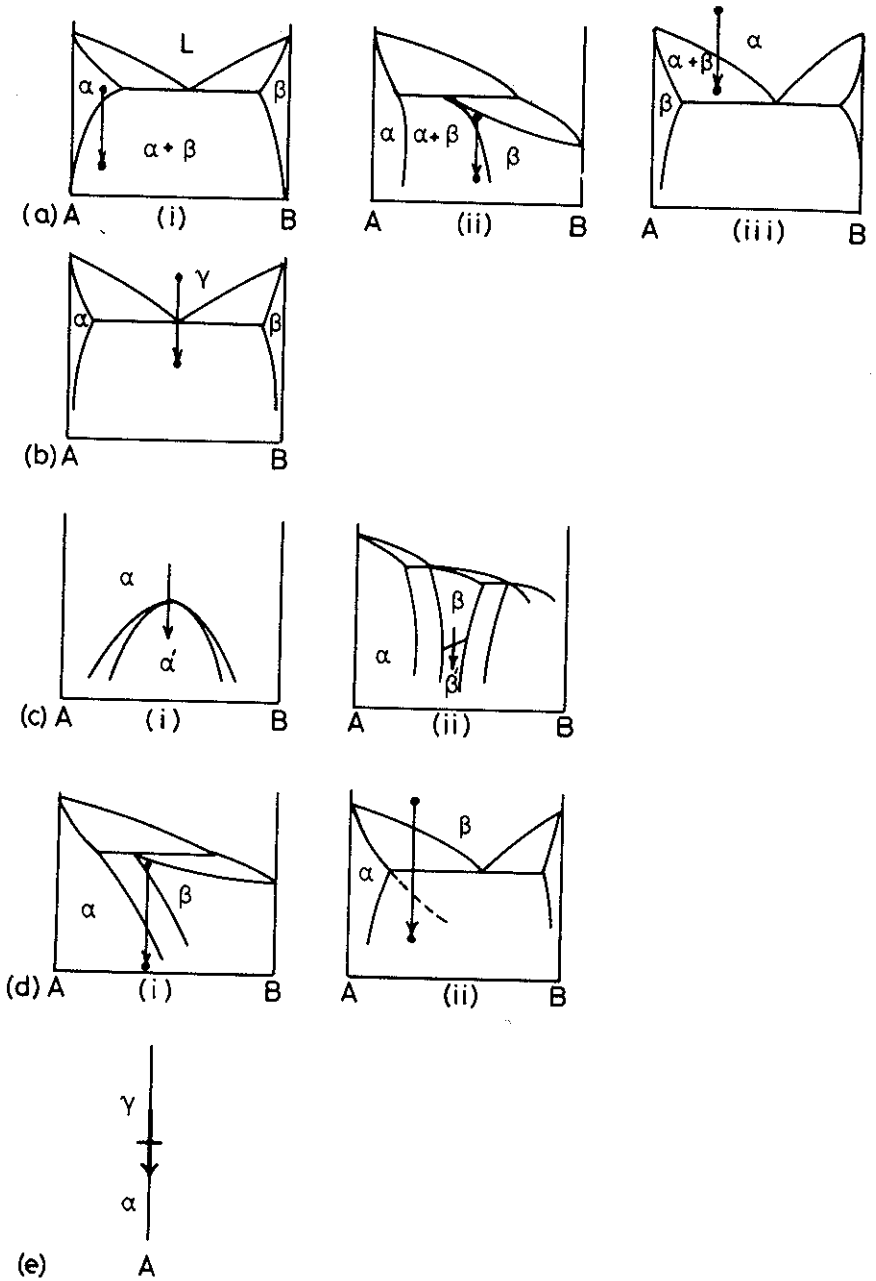

Fig. 5.1 Examples of different categories of diffusional phase transformations: (a) precipitation; (b) eutectoid; (c) ordering; (d) massive; (e) polymorphic (single component).

where only one new phase results. Note that the new β phase can either be stable (Fig. 5.1d(i)) or metastable (Fig. 5.1d(ii)).

Polymorphic transformations occur in single component systems when different crystal structures are stable over different temperature ranges, Fig. 5.1e. The most well-known of these in metallurgy are the transformations between fcc- and bcc-Fe. In practice, however, such transformations are of little practical interest and have not been extensively studied.

Apart from a few exceptions the above transformations all take place by diffusional nucleation and growth. As with solidification, nucleation is usually heterogeneous, but for the sake of simplicity let us begin by considering homogeneous nucleation.

5.1 Homogeneous Nucleation in Solids

To take a specific example consider the precipitation of B-rich β from a supersaturated A-rich α solid solution as shown in Fig. 5.1a(i). For the nucleation of β, B-atoms within the α matrix must first diffuse together to form a small volume with the β composition, and then, if necessary, the atoms must rearrange into the β crystal structure. As with the liquid → solid transformation an α/β interface must be created during the process and this leads to an activation energy barrier.

The free energy change associated with the nucleation process will have the following three contributions.

1. At temperatures where the β phase is stable, the creation of a volume V of β will cause a volume free energy *reduction* of $V\Delta G_v$.
2. Assuming for the moment that the α/β interfacial energy is isotropic the creation of an area A of interface will give a free energy *increase* of $A\gamma$.
3. In general the transformed volume will not fit perfectly into the space originally occupied by the matrix and this gives rise to a misfit strain energy ΔG_s per unit volume of β. (It was shown in Chapter 3 that, for both coherent and incoherent inclusions, ΔG_s is proportional to the volume of the inclusion.) Summing all of these gives the total free energy change as

$$\Delta G = -V\Delta G_v + A\gamma + V\Delta G_s \tag{5.5}$$

Apart from the misfit strain energy term, Equation 5.5 is very similar to that derived for the formation of a solid nucleus in a liquid. With solid/liquid interfaces γ can be treated as roughly the same for all interfaces, but for nucleation in solids γ can vary widely from very low values for coherent interfaces to high values for incoherent interfaces. Therefore the $A\gamma$ term in Equation 5.5 should really be replaced by a summation over all surfaces of the nucleus $\Sigma\gamma_i A_i$.

If we ignore the variation of γ with interface orientation and assume the nucleus is spherical with a radius of curvature r Equation 5.5 becomes

$$\Delta G = -\frac{4}{3}\pi r^3(\Delta G_v - \Delta G_s) + 4\pi r^2\gamma \tag{5.6}$$

This is shown as a function of r in Fig. 5.2. Note that the effect of the misfit strain energy is to reduce the effective driving force for the transformation to $(\Delta G_v - \Delta G_s)$. Similar curves would in fact be obtained for any nucleus shape as a function of its size. Differentiation of Equation 5.6 yields

$$r^* = \frac{2\gamma}{(\Delta G_v - \Delta G_s)} \tag{5.7}$$

$$\Delta G^* = \frac{16\pi\gamma^3}{3(\Delta G_v - \Delta G_s)^2} \tag{5.8}$$

which is very similar to the expressions for solidification, except now the chemical driving force ΔG_v is reduced by a positive strain energy term.

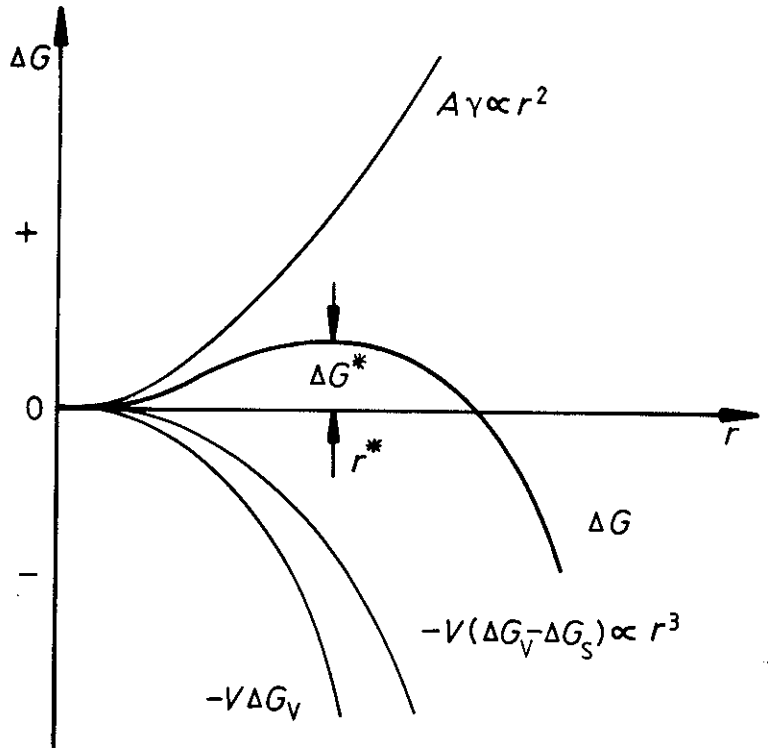

Fig. 5.2 The variation of ΔG with r for a homogeneous nucleus. There is an activation energy barrier ΔG^*.

As discussed in Chapter 4 the concentration of critical-sized nuclei C^* will be given by

$$C^* = C_0 \exp(-\Delta G^*/kT) \tag{5.9}$$

where C_0 is the number of atoms per unit volume in the phase. If each nucleus can be made supercritical at a rate of f per second the homogeneous nucleation rate will be given by

$$N_{hom} = fC^* \tag{5.10}$$

f depends on how frequently a critical nucleus can receive an atom from the α matrix. This will depend on the surface area of the nucleus and the rate at which diffusion can occur. If the activation energy for atomic migration is ΔG_m per atom, f can be written as $\omega \exp(-\Delta G_m/kT)$ where ω is a factor that includes the vibration frequency of the atoms and the area of the critical nucleus. The nucleation rate will therefore be of the form

$$N_{hom} = \omega C_0 \exp\left(-\frac{\Delta G_m}{kT}\right) \exp\left(-\frac{\Delta G^*}{kT}\right) \tag{5.11}$$

This is essentially identical to Equation 4.12 except that the temperature dependence of f has been taken into account. In order to evaluate this equation as a function of temperature ω and ΔG_m can be assumed to be constant, but ΔG^* will be strongly temperature dependent. The main factor controlling ΔG^* is the driving force for precipitation ΔG_v, Equation 5.8. Since composition is variable the magnitude of ΔG_v must be obtained from the free energy–composition diagram.

If the alloy X_0 in Fig. 5.3, is solution treated at T_1 and then cooled rapidly to T_2 it will become supersaturated with B and will try to precipitate β. When the transformation to $\alpha + \beta$ is complete the free energy of the alloy will have decreased by an amount ΔG_0 per mole as shown in Fig. 5.3b. ΔG_0 is therefore the total driving force for the transformation. However, it is not the driving force for *nucleation*. This is because the first nuclei to appear do not significantly change the α composition from X_0. The free energy released per mole of nuclei formed can be obtained as follows.

If a small amount of material with the nucleus composition (X_B^β) is removed from the α phase, the total free energy of the system will *decrease* by ΔG_1 where

$$\Delta G_1 = \mu_A^\alpha X_A^\beta + \mu_B^\alpha X_B^\beta \quad \text{(per mol } \beta \text{ removed)} \tag{5.12}$$

This follows simply from the definition of chemical potential given by Equation 1.29. ΔG_1 is a quantity represented by point P in Fig. 5.3b. If these atoms are now rearranged into the β crystal structure and replaced, the total free energy of the system will *increase* by an amount

$$\Delta G_2 = \mu_A^\beta X_A^\beta + \mu_B^\beta X_B^\beta \quad \text{(per mol } \beta \text{ formed)} \tag{5.13}$$

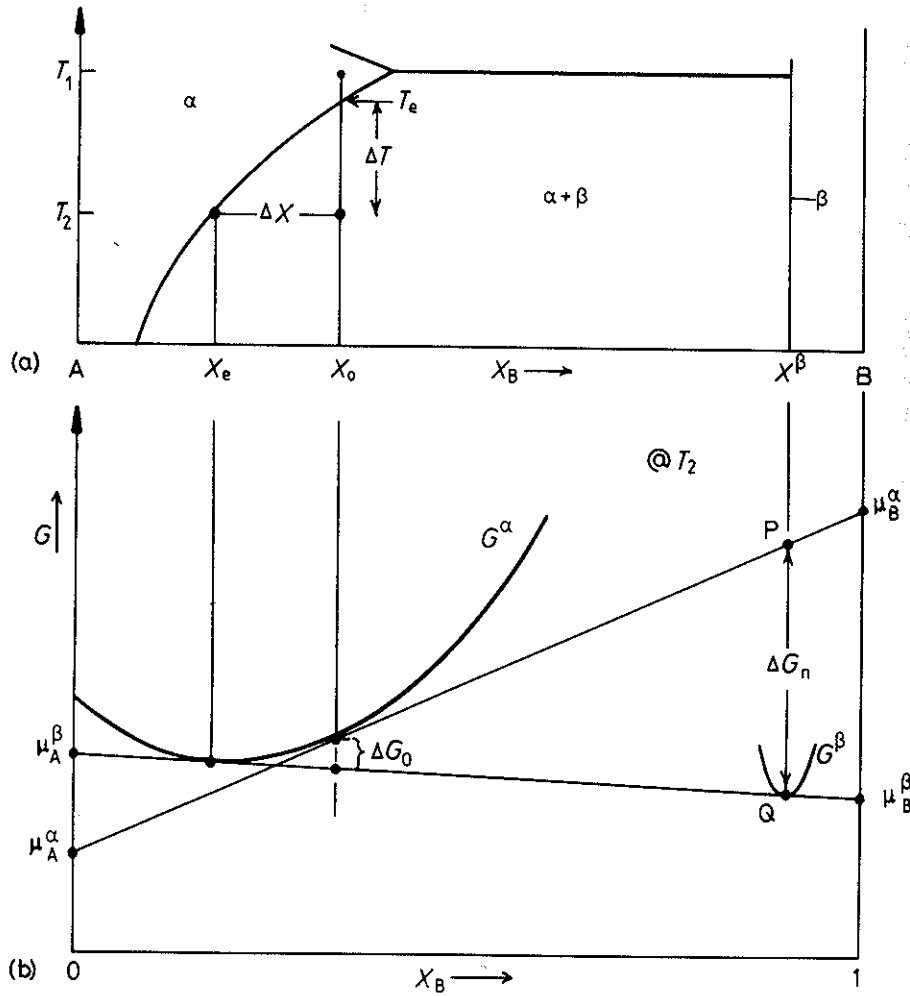

Fig. 5.3 Free energy changes during precipitation. The driving force for the first precipitates to nucleate is $\Delta G_n = \Delta G_v V_m$. ΔG_0 is the total decrease in free energy when precipitation is complete and equilibrium has been reached.

which is given by point Q. Therefore the driving force for nucleation

$$\Delta G_n = \Delta G_2 - \Delta G_1 \quad \text{per mol of } \beta \tag{5.14}$$

which is just the length PQ in Fig. 5.3b. The *volume* free energy decrease associated with the nucleation event is therefore simply given by

$$\Delta G_v = \frac{\Delta G_n}{V_m} \quad \text{per unit volume of } \beta \tag{5.15}$$

where V_m is the molar volume of β. For dilute solutions it can be shown that

approximately

$$\Delta G_v \propto \Delta X \tag{5.16}$$

where

$$\Delta X = X_0 - X_e \tag{5.17}$$

From Fig. 5.3a therefore it can be seen that the driving force for precipitation increases with increasing undercooling (ΔT) below the equilibrium solvus temperature T_e.

It is now possible to evaluate Equation 5.11 for alloy X_0 as a function of temperature. The variation of ΔG_v with temperature is shown schematically in Fig. 5.4b. After taking into account the misfit strain energy term ΔG_s the

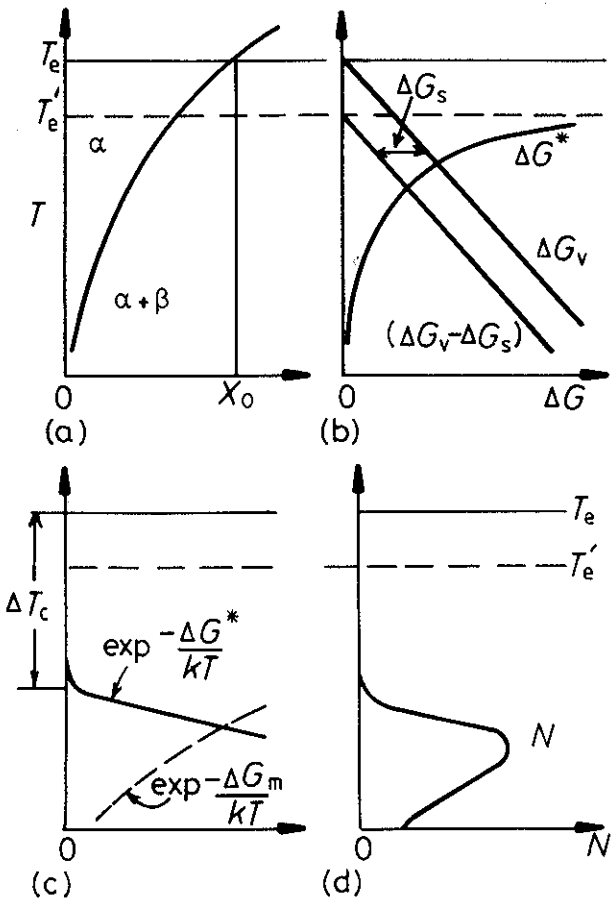

Fig. 5.4 How the rate of homogeneous nucleation varies with undercooling for alloy X_0. (a) The phase diagram. (b) The effective driving force ($\Delta G_v - \Delta G_s$) and the resultant energy barrier ΔG^*. (c) The two exponential terms that determine N as shown in (d).

effective driving force becomes ($\Delta G_v - \Delta G_s$) and the effective equilibrium temperature is reduced to T'_e. Knowing ($\Delta G_v - \Delta G_s$) the activation energy ΔG^* can be calculated from Equation 5.8 as shown. Figure 5.4c shows the two exponential terms in Equation 5.11; exp ($-\Delta G^*/kT$) is essentially the potential concentration of nuclei and, as with nucleation in liquids, this is essentially zero until a critical undercooling ΔT_c is reached, after which it rises very rapidly. The other term, exp ($-\Delta G_m/kT$), is essentially the atomic mobility. Since ΔG_m is constant this decreases rapidly with decreasing temperature. The combination of these terms, i.e. the homogeneous nucleation rate is shown in Fig. 5.4d. Note that at undercoolings smaller than ΔT_c, N is negligible because the driving force ΔG_v is too small, whereas at very high undercoolings N is negligible because diffusion is too slow. A maximum nucleation rate is obtained at intermediate undercoolings. For alloys containing less solute the critical supercooling will not be reached until lower absolute temperatures where diffusion is slower. The resultant variation of N with T in these alloys will therefore appear as shown in Fig. 5.5.

In the above treatment of nucleation it has been assumed that the nucleation rate is constant. In practice however the nucleation rate will initially be low, then gradually rise, and finally decrease again as the first nuclei to form start growing and thereby reduce the supersaturation of the remaining α.

It has also been assumed that the nuclei are spherical with the equilibrium composition and structure of the β phase. However, in practice nucleation will be dominated by whatever nucleus has the minimum activation energy barrier ΔG^*. Equation 5.8 shows that by far the most effective way of minimizing ΔG^* is by the formation of nuclei with the smallest total interfacial energy. In fact this criterion is dominating in nucleation processes. Incoherent nuclei have such a high value of γ that incoherent homogeneous nucleation is virtually impossible. If, however, the nucleus has an *orientation relationship* with the matrix, and coherent interfaces are formed, ΔG^* is greatly reduced

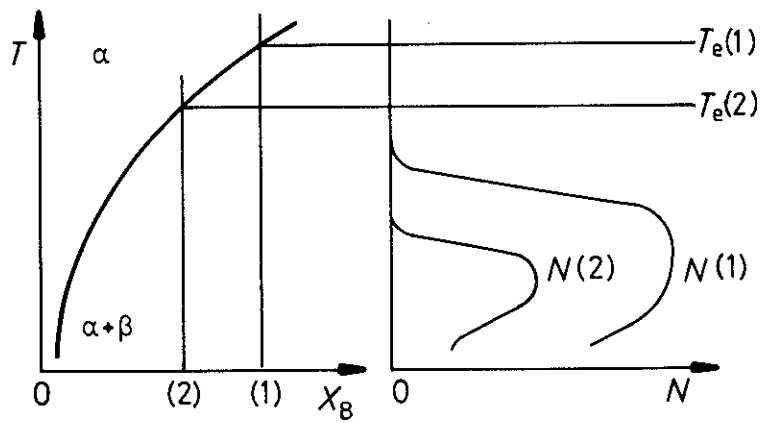

Fig. 5.5 The effect of alloy composition on the nucleation rate. The nucleation rate in alloy 2 is always less than in alloy 1.

and homogeneous nucleation becomes feasible. The formation of a coherent nucleus will of course increase ΔG_s which decreases T'_e. But below T'_c the decrease in γ resulting from coherency can more than compensate for the increase in ΔG_s. Also, by choosing a suitable shape it is often possible to minimize ΔG_s as discussed in Section 3.4.3.

In most systems the α and β phases have such different crystal structures that it is impossible to form coherent low-energy interfaces and homogeneous nucleation of the equilibrium β phase is then impossible. However, it is often possible to form a coherent nucleus of some other, metastable phase (β′) which is not present in the equilibrium phase diagram. The most common example of this is the formation of GP zones which will be discussed in more detail later.

There are a few systems in which the equilibrium phase may nucleate homogeneously. For example in the Cu–Co system Cu alloys containing 1–3% Co can be solution treated and quenched to a temperature where Co precipitates. Both Cu and Co are fcc with only a 2% difference in lattice parameter. Therefore very little coherency strain is associated with the formation of coherent Co particles. The interfacial energy is about 200 mJ m^{-2} and the critical undercooling for measurable homogeneous nucleation is about 40 °C. This system has been used to experimentally test the theories of homogeneous nucleation and reasonably close agreement was found[1].

Another system in which the equilibrium phase is probably formed homogeneously at a few tens of degrees undercooling is the precipitation of Ni_3Al in many Ni-rich alloys. Depending on the system the misfit varies up to a maximum of 2%, and γ is probably less than 30 mJ m^{-2}. Most other examples of homogeneous nucleation, however, are limited to metastable phases, usually GP zones. (See Section 5.5.1.)

5.2 Heterogeneous Nucleation

Nucleation in solids, as in liquids, is almost always heterogeneous. Suitable nucleation sites are non-equilibrium defects such as excess vacancies, dislocations, grain boundaries, stacking faults, inclusions, and free surfaces, all of which increase the free energy of the material. If the creation of a nucleus results in the destruction of a defect, some free energy (ΔG_d) will be released thereby reducing (or even removing) the activation energy barrier. The equivalent to Equation 5.5 for heterogeneous nucleation is

$$\Delta G_{het} = -V(\Delta G_v - \Delta G_s) + A\gamma - \Delta G_d \qquad (5.18)$$

Nucleation on Grain Boundaries

Ignoring any misfit strain energy, the optimum embryo shape should be that which minimizes the total interfacial free energy. The optimum shape for an *incoherent* grain-boundary nucleus will consequently be two abutted spherical

caps as shown in Fig. 5.6, with θ given by

$$\cos\theta = \gamma_{\alpha\alpha}/2\gamma_{\alpha\beta} \tag{5.19}$$

(assuming $\gamma_{\alpha\beta}$ is isotropic and equal for both grains). The excess free energy associated with the embryo will be given by

$$\Delta G = -V\Delta G_v + A_{\alpha\beta}\gamma_{\alpha\beta} - A_{\alpha\alpha}\gamma_{\alpha\alpha} \tag{5.20}$$

where V is the volume of the embryo, $A_{\alpha\beta}$ is the area of α/β interface of energy $\gamma_{\alpha\beta}$ created, and $A_{\alpha\alpha}$ the area of α/α grain boundary of energy $\gamma_{\alpha\alpha}$ destroyed during the process. The last term of the above equation is simply ΔG_d in Equation 5.18.

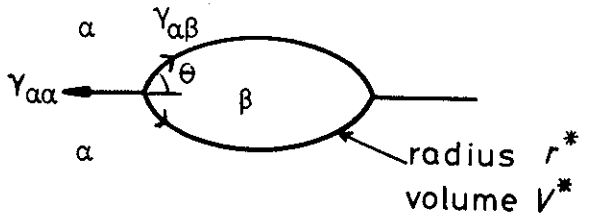

Fig. 5.6 The critical nucleus size (V^*) for grain boundary nucleation.

It can be seen that grain boundary nucleation is analogous to solidification on a substrate (Section 4.1.3) and the same results will apply. Again the critical radius of the spherical caps will be independent of the grain boundary and given by

$$r^* = 2\gamma_{\alpha\beta}/\Delta G_v \tag{5.21}$$

and the activation energy barrier for heterogeneous nucleation will be given by

$$\frac{\Delta G^*_{het}}{\Delta G^*_{hom}} = \frac{V^*_{het}}{V^*_{hom}} = S(\theta) \tag{5.22}$$

where $S(\theta)$ is a shape factor given by

$$S(\theta) = \frac{1}{2}(2 + \cos\theta)(1 - \cos\theta)^2 \tag{5.23}$$

The ability of a grain boundary to reduce ΔG^*_{het}, i.e. its potency as a nucleation site, depends on cos θ, i.e. on the ratio $\gamma_{\alpha\alpha}/2\gamma_{\alpha\beta}$.

V^* and ΔG^* can be reduced even further by nucleation on a grain edge or grain corner, Figs. 5.7 and 5.8. Figure 5.9 shows how $\Delta G^*_{het}/\Delta G^*_{hom}$ depends on cos θ for the various grain boundary nucleation sites.

High-angle grain boundaries are particularly effective nucleation sites for incoherent precipitates with high $\gamma_{\alpha\beta}$. If the matrix and precipitate are sufficiently compatible to allow the formation of lower energy facets then V^* and

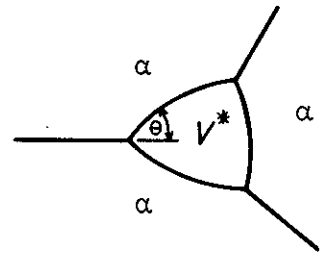

Fig. 5.7 Critical nucleus shape for nucleation on a grain edge.

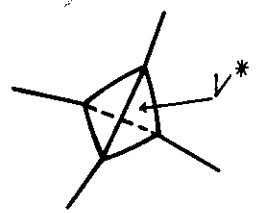

Fig. 5.8 Critical nucleus shape for nucleation on a grain corner.

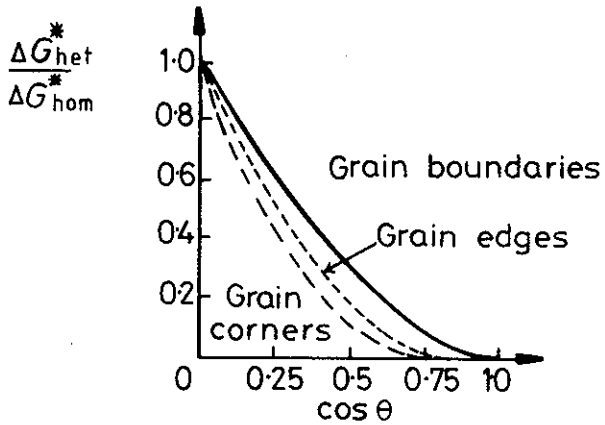

Fig. 5.9 The effect of θ on the activation energy for grain boundary nucleation relative to homogeneous nucleation. (After J.W. Cahn, *Acta Metallurgia* **4** (1956) 449.)

ΔG^*_{het} can be further reduced as shown in Fig. 5.10. The nucleus will then have an orientation relationship with one of the grains. Such nuclei are to be expected whenever possible, since the most successful nuclei, i.e. those which form most rapidly, will have the smallest nucleation barrier.

Other planar defects such as inclusion/matrix interfaces, stacking faults and free surfaces can behave in a similar way to grain boundaries in reducing ΔG^*. Note, however, that stacking faults are much less potent sites due to their lower energy in comparison to high-angle boundaries.

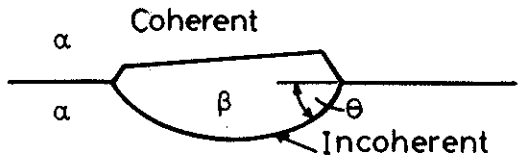

Fig. 5.10 The critical nucleus size can be reduced even further by forming a low-energy coherent interface with one grain.

Dislocations

The lattice distortion in the vicinity of a dislocation can assist nucleation in several ways. The main effect of dislocations is to reduce the ΔG_s-contribution to ΔG^* by reducing the total strain energy of the embryo. A coherent nucleus with a negative misfit, i.e. a smaller volume than the matrix, can reduce its ΔG^* by forming in the region of compressive strain above an edge dislocation, whereas if the misfit is positive it is energetically favourable for it to form below the dislocation.

Nucleation on dislocations may also be assisted by solute segregation which can raise the composition of the matrix to nearer that of the precipitate. The dislocation can also assist in growth of an embryo beyond the critical size by providing a diffusion pipe with a lower ΔG_m.

Dislocations are not very effective for reducing the interfacial energy contribution to ΔG^*. This means that nucleation on dislocations usually requires rather good matching between precipitate and matrix on at least one plane, so that low-energy coherent or semicoherent interfaces can form. Ignoring strain energy effects, the minimum ΔG^* is then achieved when the nucleus shape is the equilibrium shape given by the Wulff construction. When the precipitate and matrix have different crystal structures the critical nucleus should therefore be disc-like or needle-like as discussed in Section 3.4.2.

In fcc crystals the $\frac{a}{2}\langle 110\rangle$ unit dislocations can dissociate to produce a ribbon of stacking fault, e.g.

$$\frac{a}{2}[110] \rightarrow \frac{a}{6}[121] + \frac{a}{6}[21\bar{1}]$$

giving a stacking fault on $(1\bar{1}1)$ separated by two Shockley partials. Since the stacking fault is in effect four close-packed layers of hcp crystal (Fig 3.59b) it can act as a very potent nucleation site for an hcp precipitate. This type of nucleation has been observed for the precipitation of the hexagonal transition phase γ' in Al–Ag alloys. Nucleation is achieved simply by the diffusion of silver atoms to the fault. Thus there will automatically be an orientation relationship between the γ' precipitate (fault) and the matrix of the type

$$(0001)_{\gamma'}//(1\bar{1}1)_\alpha$$
$$[11\bar{2}0]_{\gamma'}//[110]_\alpha$$

which ensures good matching and low energy interfaces.

It should be noted that even in annealed specimens dislocation densities are often sufficiently high to account for any precipitate dispersion that is resolvable in the light microscope, i.e. $\sim 1\ \mu m^{-2}$. Figure 5.11 shows an example of niobium carbonitride precipitates on dislocations in a ferritic iron matrix. This is a so-called dark-field electron microscope micrograph in which the precipitates are imaged bright and the matrix dark. The precipitates lie in rows along dislocations.

Excess Vacancies

When an age-hardening alloy is quenched from a high temperature, excess vacancies are retained during the quench. These vacancies can assist nucleation by increasing diffusion rates, or by relieving misfit strain energies. They may influence nucleation either individually or collectively by grouping into small clusters.

Since ΔG_d is relatively small for vacancies, nucleation will only take place when a reasonable combination of the following conditions is met: low interfacial energy (i.e. fully coherent nuclei), small volume strain energy, and

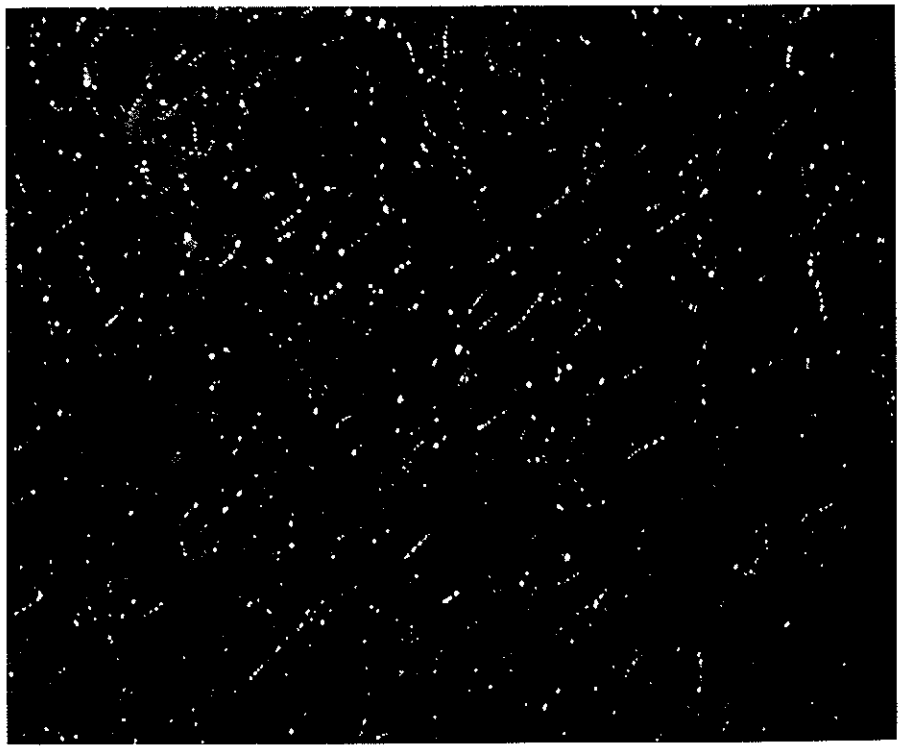

Fig. 5.11 Rows of niobium carbonitride precipitates on dislocations in ferrite (× 108 000). (Dark-field electron micrograph in which the precipitates show up bright.)

high driving force. These are essentially the same conditions that must be fulfilled for homogeneous nucleation. Since individual vacancies or small clusters cannot be resolved with conventional transmission electron microscopy, evidence for the role of vacancies as hetergenous nucleation sites is indirect (discussed later).

5.2.1 *Rate of Heterogeneous Nucleation*

If the various nucleation sites are arranged in order of increasing ΔG_d, i.e. decreasing ΔG^*, the sequence would be roughly

1. homogeneous sites
2. vacancies
3. dislocations
4. stacking faults
5. grain boundaries and interphase boundaries
6. free surfaces.

Nucleation should always occur most rapidly on sites near the bottom of the list. However the relative importance of these sites in determining the overall rate at which the alloy will transform also depends on the relative concentrations of the sites. For homogeneous nucleation every atom is a potential nucleation site, whereas only those atoms on grain boundaries, for example, can take part in boundary-assisted nucleation.

If the concentration of heterogeneous nucleation sites is C_1 *per unit volume*, the heterogeneous nucleation rate will be given by an equation of the form

$$N_{het} = \omega C_1 \exp\left(-\frac{\Delta G_m}{kT}\right) \cdot \exp\left(-\frac{\Delta G^*}{kT}\right) \quad \text{nuclei m}^{-3}\text{s}^{-1} \tag{5.24}$$

This is plotted as a function of temperature in Fig. 5.12. Note that, as with heterogeneous nucleation in liquids, measurably high nucleation rates can be

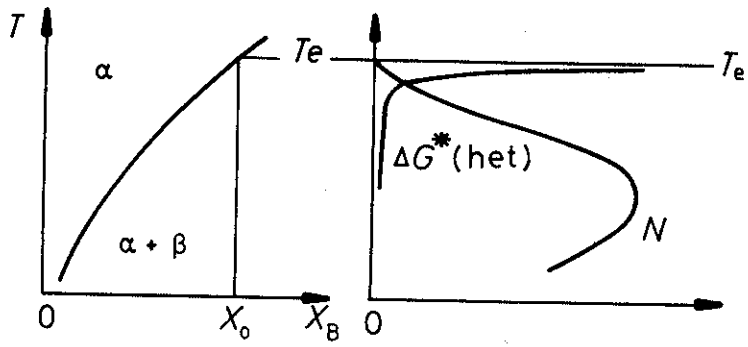

Fig. 5.12 The rate of heterogeneous nucleation during precipitation of β in alloy X_0 as a function of undercooling.

obtained at very small driving forces. The relative magnitudes of the heterogeneous and homogeneous volume nucleation rates can be obtained by dividing Equation 5.11 by 5.24 giving

$$\frac{N_{het}}{N_{hom}} = \frac{C_1}{C_0} \exp\left(\frac{\Delta G^*_{hom} - \Delta G^*_{het}}{kT}\right) \tag{5.25}$$

(Differences in ω and ΔG_m are not so important and have been ignored.) Since ΔG^* is always smallest for heterogeneous nucleation the exponential factor in the above equation is always a large quantity which favours a high heterogeneous nucleation rate. However, the factor (C_1/C_0) must also be taken into account, i.e. the number of atoms on heterogeneous sites relative to the number within the matrix. For grain boundary nucleation

$$\frac{C_1}{C_0} = \frac{\delta}{D} \tag{5.26}$$

where δ is the boundary thickness and D is the grain size. For nucleation on grain edges and corners (C_1/C_0) becomes reduced even further to $(\delta/D)^2$ and $(\delta/D)^3$. Therefore for a 50 μm grain size taking δ as 0.5 nm gives $\delta/D \simeq 10^{-5}$. Consequently grain boundary nucleation will dominate over homogeneous nucleation if the boundary is sufficiently potent to make the exponential term in Equation 5.23 greater than 10^5. Values for C_1/C_0 for other sites are listed in Table 5.1.

In general the type of site which gives the highest volume nucleation rate will depend on the driving force (ΔG_v). At very small driving forces, when activation energy barriers for nucleation are high, the highest nucleation rates will be produced by grain-corner nucleation. As the driving force increases, however, grain edges and then boundaries will dominate the transformation. At very high driving forces it may be possible for the (C_1/C_0) term to dominate and then homogeneous nucleation provides the highest nucleation rates. Similar considerations will apply to the relative importance of other heterogeneous nucleation sites.

The above comments concerned nucleation during isothermal transformations when the specimen is held at a constant temperature. If nucleation occurs during continuous cooling the driving force for nucleation will increase with time. Under these conditions the initial stages of the transformation will be dominated by those nucleation sites which can first produce a measurable volume nucleation rate. Considering only grain boundaries again, if $\gamma_{\alpha\alpha}/\gamma_{\alpha\beta}$ is high, noticeable transformation will begin first at the grain corners, whereas if the grain boundary is less potent ($\gamma_{\alpha\alpha}/\gamma_{\alpha\beta}$ smaller) nucleation may not be possible until such high driving forces are reached that less favourable heterogeneous or even homogeneous nucleation sites dominate. This will not of course exclude precipitation on potent heterogeneous sites, but they will make only a very small contribution to the total nucleation rate.

As explained above, the successful critical nuclei are those with the smallest nucleation barrier, i.e. the smallest critical volume. In the absence of strain-energy effects the precipitate shape satisfying this criterion is that which minimizes the total interfacial free energy. Thus nuclei will usually be bounded by a combination of coherent or semicoherent facets and smoothly curved incoherent interfaces. For the precipitate to grow these interfaces must migrate and the shape that develops during growth will be determined by the relative migration rates. As explained in Section 3.5.1, when the two phases have different crystal structures semicoherent interfaces have very low mobility and are forced to migrate by a ledge mechanism. Incoherent interfaces on the other hand are highly mobile. If there are problems in maintaining a constant supply of ledges the incoherent interfaces will be able to advance faster than the semicoherent interface and a nucleus with one plane of good matching should grow into a thin disc or plate as shown in Fig. 5.13. This is the origin of the so-called Widmanstätten morphology[12].

The next few sections will be concerned with developing an approximate quantitative treatment for the ledge mechanism and for the rate of migration of curved incoherent interfaces, but before treating these two cases it is useful to begin with the simpler case of a planar incoherent interface.

Fig. 5.13 The effect of interface type on the morphology of a growing precipitate. (A) Low-mobility semicoherent interfaces. (B) High-mobility incoherent interfaces.

5.3.1 *Growth behind Planar Incoherent Interfaces*

It will be apparent from the above discussion that planar interfaces in crystalline solids will usually not be incoherent. However, one situation where approximately planar incoherent interfaces may be found is after grain-boundary nucleation. If many incoherent nuclei form on a grain boundary they might subsequently grow together to form a slab of β precipitate as shown in Fig. 5.14.

Imagine that such a slab of solute-rich precipitate has grown from zero thickness and that the instantaneous growth rate is v. Since the concentration of solute in the precipitate (C_β) is higher than in the bulk (C_0) the matrix adjacent to the precipitate will be depleted of solute as shown. Also since the interface is incoherent diffusion-controlled growth and local equilibrium at

Table 5.1 C_1/C_0 for Various Heterogeneous Nucleation Sites

Grain boundary	Grain edge	Grain corner	Dislocations		Excess vacancies
$D = 50$ μm	$D = 50$ μm	$D = 50$ μm	10^5 mm^{-2}	10^8 mm^{-2}	$X_v = 10^{-6}$
10^{-5}	10^{-10}	10^{-15}	10^{-8}	10^{-5}	10^{-6}

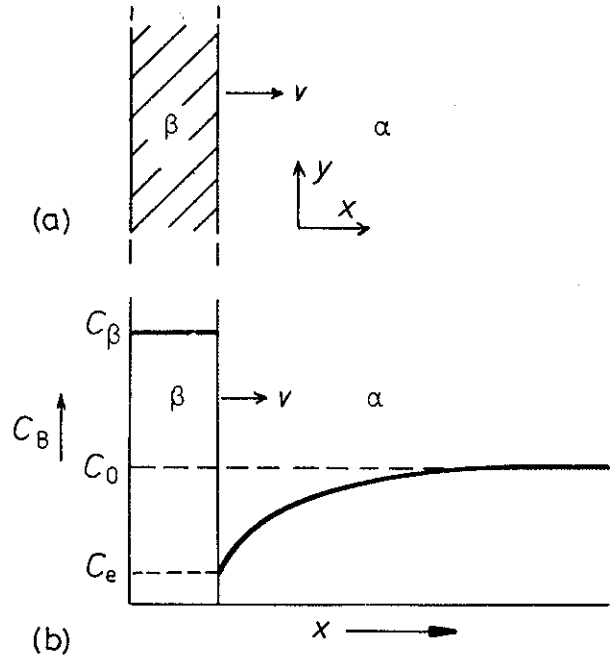

Fig. 5.14 Diffusion-controlled thickening of a precipitate plate.

the interface can be assumed, i.e. the solute concentration in the matrix adjacent to the β will be the equilibrium value C_e. The growth rate (v) will depend on the concentration gradient at the interface dC/dx.

For unit area of interface to advance a distance dx a volume of material $1 \cdot dx$ must be converted from α containing C_e to β containing C_β moles of B per unit volume, i.e. $(C_\beta - C_e)dx$ moles of B must be supplied by diffusion through the α. The flux of B through unit area in time dt is given by $D(dC/dx)dt$, where D is the *interdiffusion* coefficient (or interstitial diffusion coefficient). Equating these two quantities gives

$$v = \frac{dx}{dt} = \frac{D}{C_\beta - C_e} \cdot \frac{dC}{dx} \tag{5.27}$$

As the precipitate grows solute must be depleted from an ever-increasing volume of matrix so that dC/dx in the above equation decreases with time. To make this quantitative, consider a simplified approach originally due to Zener[2]. If the concentration profile is simplified to that shown in Fig. 5.15 dC/dx is given by $\Delta C_0/L$ where $\Delta C_0 = C_0 - C_e$. The width of the diffusion zone L can be obtained by noting that the conservation of solute requires the two shaded areas in Fig. 5.15 to be equal, i.e.

$$(C_\beta - C_0)x = L\Delta C_0/2$$

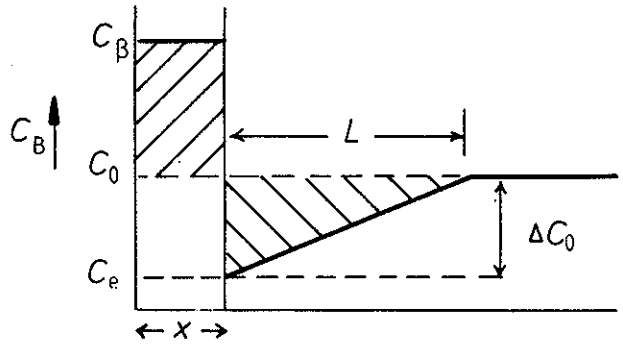

Fig. 5.15 A simplification of the concentration profile.

where x is the thickness of the slab. The growth rate therefore becomes

$$v = \frac{D(\Delta C_0)^2}{2(C_\beta - C_e)(C_\beta - C_0)x} \tag{5.28}$$

If it is assumed that the molar volume (V_m) is a constant, the concentrations in the above equation can be replaced by mole fractions ($X = CV_m$). Furthermore, for the sake of simplicity it can often be assumed that $C_\beta - C_0 \simeq C_\beta - C_e$. Integration of Equation 5.28 then gives

$$x = \frac{\Delta X_0}{\sqrt{(X_\beta - X_e)}} \sqrt{(Dt)} \tag{5.29}$$

and

$$v = \frac{\Delta X_0}{2(X_\beta - X_e)} \sqrt{\frac{D}{t}} \tag{5.30}$$

where $\Delta X_0 = X_0 - X_e$ (Fig. 5.16) is the supersaturation prior to precipitation.

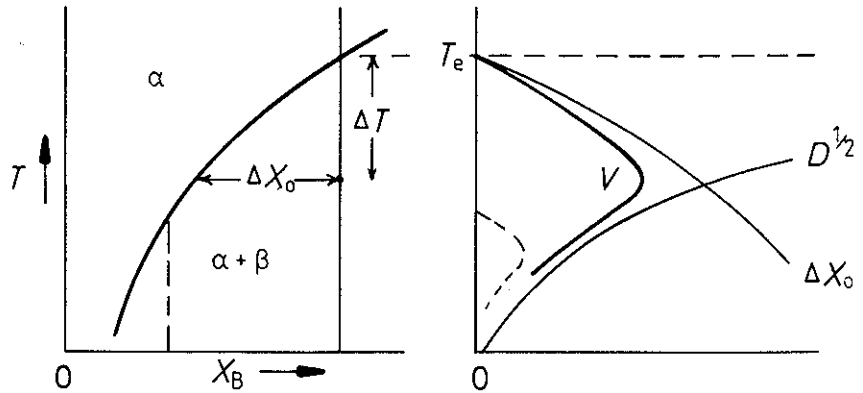

Fig. 5.16 The effect of temperature and position on growth rate, v.

The following points are important to note regarding these equations.

1. $x \propto \sqrt{(Dt)}$, i.e. precipitate thickening obeys a parabolic growth law.
2. $v \propto \Delta X_0$, i.e. for a given time the growth rate is proportional to the supersaturation.
3. $v \propto \sqrt{(D/t)}$.

The effect of alloy composition and temperature on growth rate is illustrated in Fig. 5.16. Growth rates are low at small undercoolings due to small supersaturation ΔX_0 but are also low at large undercoolings due to slow diffusion. A maximum growth rate will occur at some intermediate undercooling.

When the diffusion fields of separate precipitates begin to overlap Equation 5.30 will no longer apply, but growth will decelerate more rapidly and finally cease when the matrix concentration is X_e everywhere, Fig. 5.17.

Although these equations are only approximate and were derived for a planar interface, the conclusions are not significantly altered by more thorough treatments or by allowing curved interfaces. Thus it can be shown that

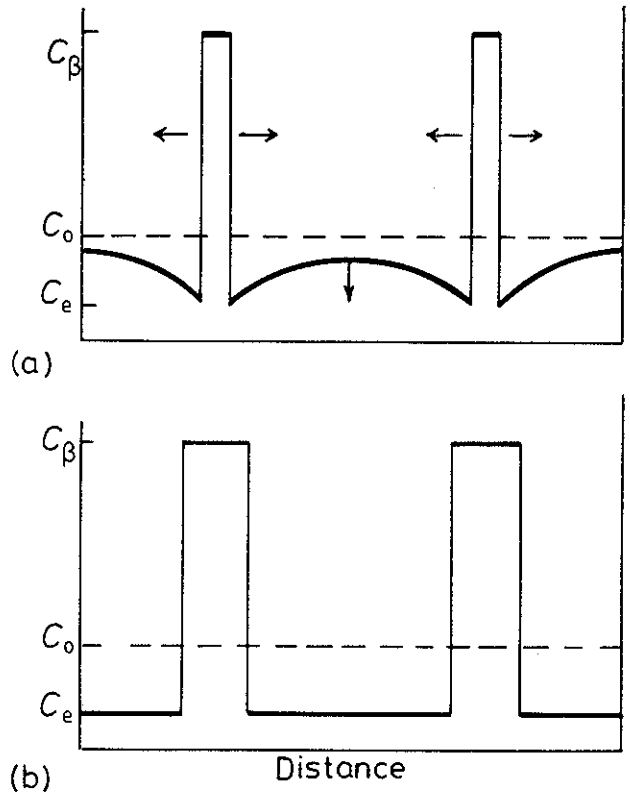

Fig. 5.17 (a) Interference of growing precipitates due to overlapping diffusion fields at later stage of growth. (b) Precipitate has stopped growing.

any linear dimension of a spheroidal precipitate increases as $\sqrt{(Dt)}$ provided all interfaces migrate under volume diffusion control.

Usually grain boundary precipitates do not form a continuous layer along the boundary but remain as isolated particles. The growth of such precipitates can occur at rates far greater than allowed by volume diffusion. The reason for this is that the grain boundary can act as a collector plate for solute as shown in Fig. 5.18.[22] Growth of such a so-called grain-boundary allotriomorph involves three steps: (1) volume diffusion of solute to the grain boundary; (2) diffusion of solute along the grain boundary with some attachment at the precipitate rim; and (3) diffusion along the α/β interfaces allowing accelerated thickening. This mechanism is of greatest significance when substitutional diffusion is involved. In the case of interstitial solutions diffusion short circuits are comparatively unimportant due to the high volume diffusion rates.

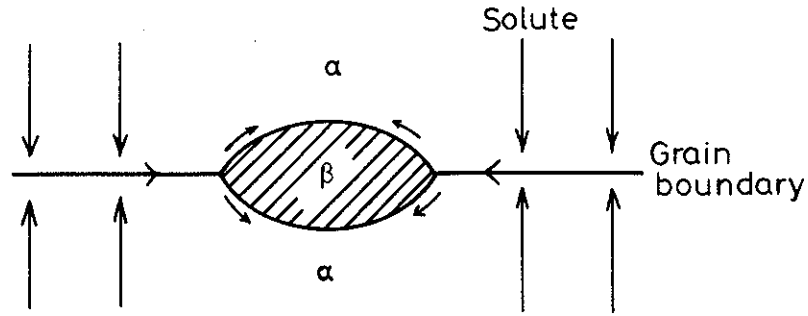

Fig. 5.18 Grain-boundary diffusion can lead to rapid lengthening and thickening of grain boundary precipitates.

5.3.2 *Diffusion-Controlled Lengthening of Plates or Needles*

Imagine now that the β precipitate is a plate of constant thickness having a cylindrically curved *incoherent* edge of radius r as shown in Fig. 5.19a. Again the concentration profile across the curved interface will appear as shown in Fig. 5.19b, but now, due to the Gibbs-Thomson effect, the equilibrium concentration in the matrix adjacent to the edge will be increased to C_r. The concentration gradient available to drive diffusion to the advancing edge is therefore reduced to $\Delta C/L$ where $\Delta C = C_0 - C_r$ and L is a characteristic diffusion distance. The diffusion problem in this case is more complex as diffusion occurs radially. However, solution of the relevant equations shows that L is given by kr where k is a numerical constant (~ 1). By analogy with Equation 5.27, therefore, the lengthening rate will be given by

$$v = \frac{D}{C_\beta - C_r} \cdot \frac{\Delta C}{kr} \tag{5.31}$$

The composition difference available to drive diffusion will depend on the tip radius as shown in Fig. 5.20. With certain simplifying assumptions it can

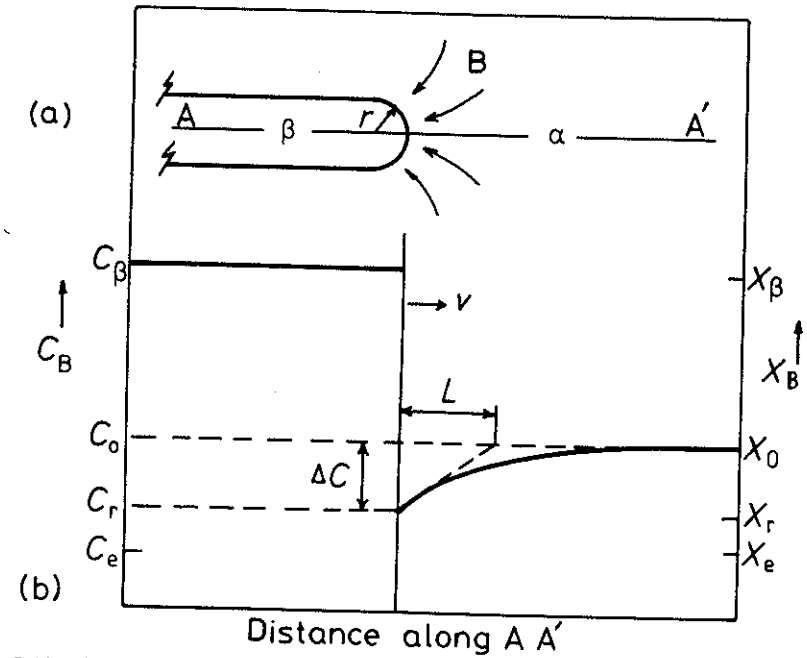

Fig. 5.19 (a) The edge of a plate-like precipitate. (b) A concentration profile along AA′ in (a).

be shown that

$$\Delta X = \Delta X_0\left(1 - \frac{r^*}{r}\right) \tag{5.32}$$

where $\Delta X = X_0 - X_r$, $\Delta X_0 = X_0 - X_e$ and r^* is the critical nucleus radius, i.e. the value of r required to reduce ΔX to zero. Again, assuming constant molar volume, the above equations can be combined to give

$$v = \frac{D\Delta X_0}{k(X_\beta - X_r)} \cdot \frac{1}{r}\left(1 - \frac{r^*}{r}\right) \tag{5.33}$$

This equation will apply as long as there is no decrease in supersaturation far from the interface due to other precipitates. The difference between this equation and Equation 5.30 is that for a given plate thickness the lengthening rate should be constant, i.e. $x \propto t$ (linear growth).

Although the above equations were developed for the lengthening of a plate, the same equations can be derived for the lengthening of a needle under diffusion-controlled growth. The only difference is that the edge of a needle has a spherical tip so that the Gibbs–Thomson increase in free energy is $2\gamma V_m/r$ instead of $\gamma V_m/r$. The value of r^* in Equation 5.33 will, therefore, be different for a plate and a needle.

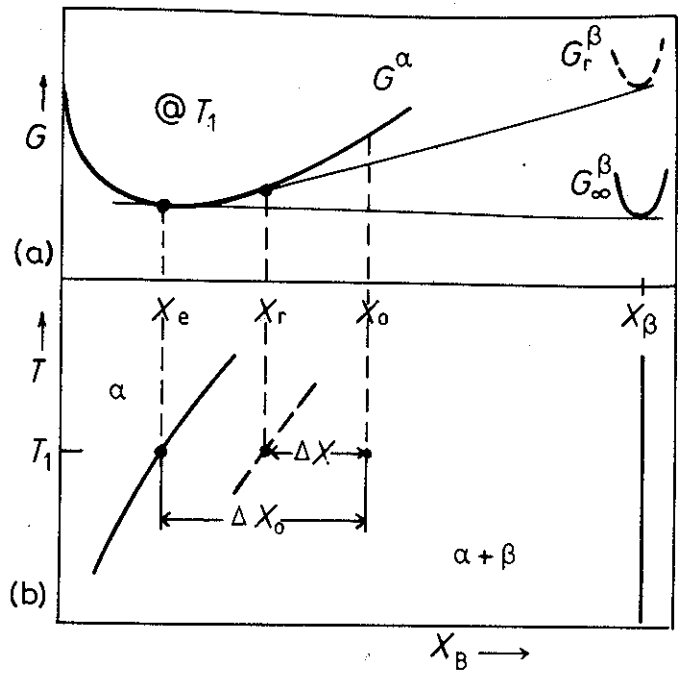

Fig. 5.20 The Gibbs-Thomson effect. (a) Free energy curves at T_1. (b) Corresponding phase diagram.

The above treatment only applies to plates or needles that lengthen by a volume diffusion-controlled continuous growth process. This is a reasonable assumption for the curved ends of needles, but in the case of plate-like precipitates the edges are often faceted and are observed to migrate by a ledge mechanism. Atoms can then only attach at the ledges and new equations must be derived as discussed below.

Another source of deviation between theory and practice is if solute can be transported to the advancing precipitate edges by short-circuit diffusion in the broad faces of the precipitate plate.

5.3.3 *Thickening of Plate-like Precipitates*

The treatment given in Section 5.3.1 for a planar incoherent interface is only valid for interfaces with high accommodation factors. In general this will not be the case for the broad faces of plate-like precipitates which are semicoherent and are restricted to migrate by the lateral movement of ledges.

For simplicity, imagine a plate-like precipitate that is thickening by the lateral movement of linear ledges of constant spacing λ and height h, Fig. 5.21. It can readily be seen that the half-thickness of the plate should

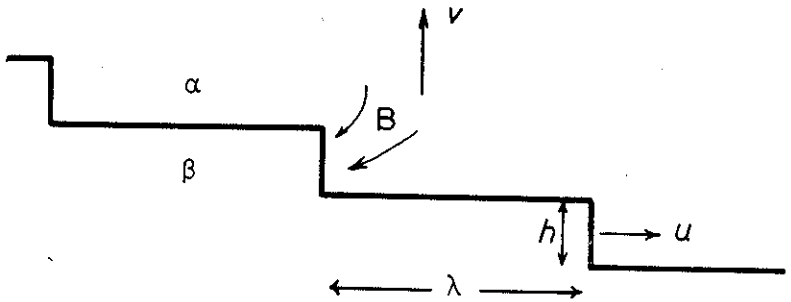

Fig. 5.21 Thickening of plate-like precipitates by ledge mechanism.

increase at a rate v given by

$$v = \frac{uh}{\lambda} \tag{5.34}$$

where u is the rate of lateral migration.

The problem of ledge migration is very similar to that of plate lengthening. The necessary composition changes required for precipitate growth must be achieved by long-range diffusion to and from the ledges as shown in Fig. 5.21. If the edges of the ledges are incoherent the matrix composition in contact with the ledges will be X_e and growth will be diffusion controlled. A similar treatment to that given in Section 5.3.2 then gives the rate of lateral migration as[3]

$$u = \frac{D\Delta X_0}{k(X_\beta - X_e)h} \tag{5.35}$$

This is essentially the same as Equation 5.33 for the lengthening of a plate with $h \simeq r$ and $X_r = X_e$, i.e. no Gibbs–Thomson effect. Combining the above equations shows that the thickening rate is independent of h and given by

$$v = \frac{D\Delta X_0}{k(X_\beta - X_e)\lambda} \tag{5.36}$$

Thus, provided the diffusion fields of different precipitates do not overlap, the rate at which plates thicken will be inversely proportional to the interledge spacing λ. The validity of Equation 5.36 is dependent on there being a constant supply of ledges. As with faceted solid/liquid interfaces, new ledges can be generated by various mechanisms such as repeated surface nucleation, spiral growth, nucleation at the precipitate edges, or from intersections with other precipitates. With the exception of spiral growth, however, none of these mechanisms can maintain a supply of ledges with constant λ.

By using hot-stage transmission electron microscopy it is possible to measure the thickening rates of individual precipitate plates. Figure 5.22 shows results obtained from a γ plate in the Al–Ag system[4]. It can be seen that there

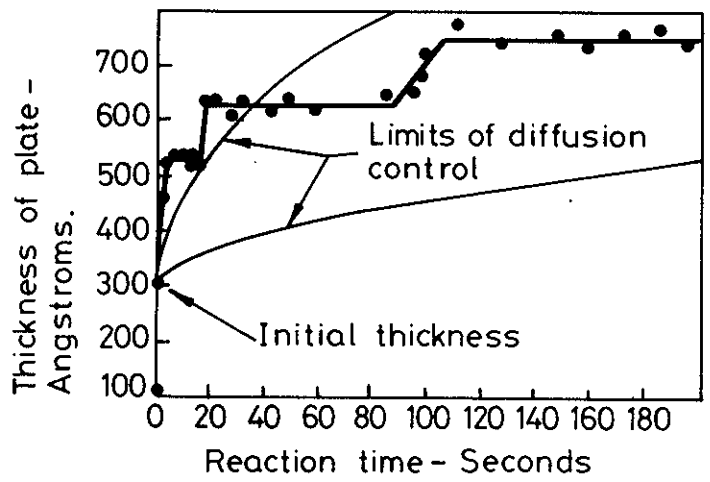

Fig. 5.22 The thickening of a γ plate in an Al–15 wt% Ag alloy at 400 °C. (From C. Laird and H.I. Aaronson, *Acta Metallurgica* **17** (1969) 505.)

are appreciable intervals of time when there is no perceptible increase in plate thickness followed by periods when the thickness increases rapidly as an interfacial ledge passes. The two smooth lines in the figure are upper and lower limits for the rate of thickening for a planar incoherent interface in the same system, assuming diffusion control. The ledge mechanism is clearly a very different process. The fact that there is no perceptible increase in thickness except when ledges pass is strong evidence in favour of the immobility of semicoherent interfaces. It can also be seen that the thickening rate is not constant implying that ledge nucleation is rate controlling.

Measurements on precipitates in other systems indicate that even within the same system the thickness/time relationship can vary greatly from plate to plate, presumably depending on differences in the ease of nucleation of new ledges.

5.4 Overall Transformation Kinetics—TTT Diagrams

The progress of an isothermal phase transformation can be conveniently represented by plotting the fraction transformation (f) as a function of time and temperature, i.e. a TTT diagram as shown in Fig. 5.23a for example. For transformations of the type $\alpha \rightarrow \beta$, f is just the volume fraction of β at any time. For precipitation reactions $\alpha' \rightarrow \alpha + \beta$, f can be defined as the volume of β at time t divided by the final volume of β. In both cases f varies from 0 to 1 from the beginning to the end of the transformation, Fig. 5.23b.

Among the factors that determine $f(t, T)$ are the nucleation rate, the growth rate, the density and distribution of nucleation sites, the overlap of diffusion fields from adjacent transformed volumes, and the impingement of

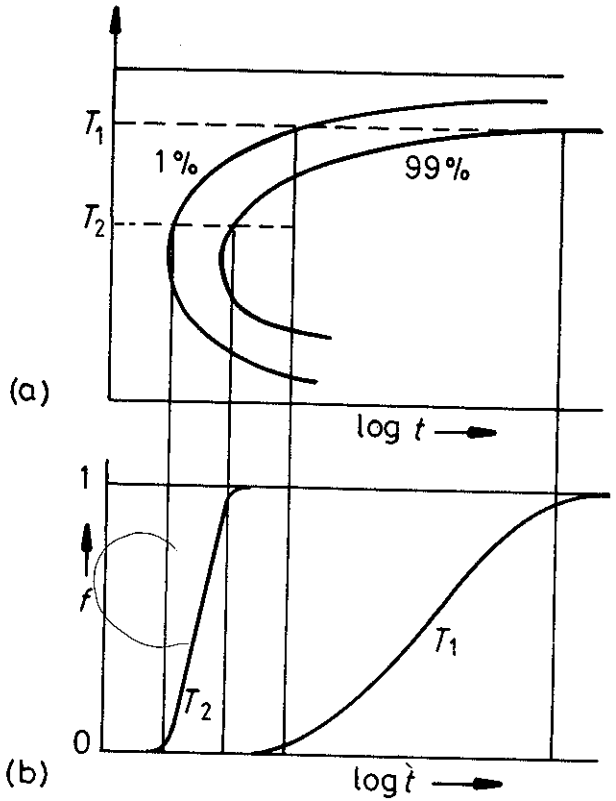

Fig. 5.23 The percentage transformation versus time for different transformation temperatures.

adjacent transformed volumes. Some of the problems involved are illustrated in Fig. 5.24. After quenching to the transformation temperature the metastable α phase will contain many nucleation sites (usually heterogeneous). One possible sequences of events, Fig. 5.24a, is that nuclei form throughout the transformation so that a wide range of particle sizes exists at any time. Another possibility is that all nuclei form right at the beginning of transformation, Fig. 5.24b. If all potential nucleation sites are consumed in the process this is known as *site saturation*. In Fig. 5.24a, f will depend on the nucleation rate and the growth rate. In Fig. 5.24b, f will only depend on the number of nucleation sites and the growth rate. For transformations of the type $\alpha \rightarrow \beta$ or $\alpha \rightarrow \beta + \gamma$ (known collectively as *cellular transformations*) all of the parent phase is consumed by the transformation product, Fig. 5.24c. In these cases the transformation does not terminate by the gradual reduction in the growth rate, but by the impingement of adjacent cells growing with a constant velocity. Pearlite, cellular precipitation, massive transformations and recrystallization belong to this category.

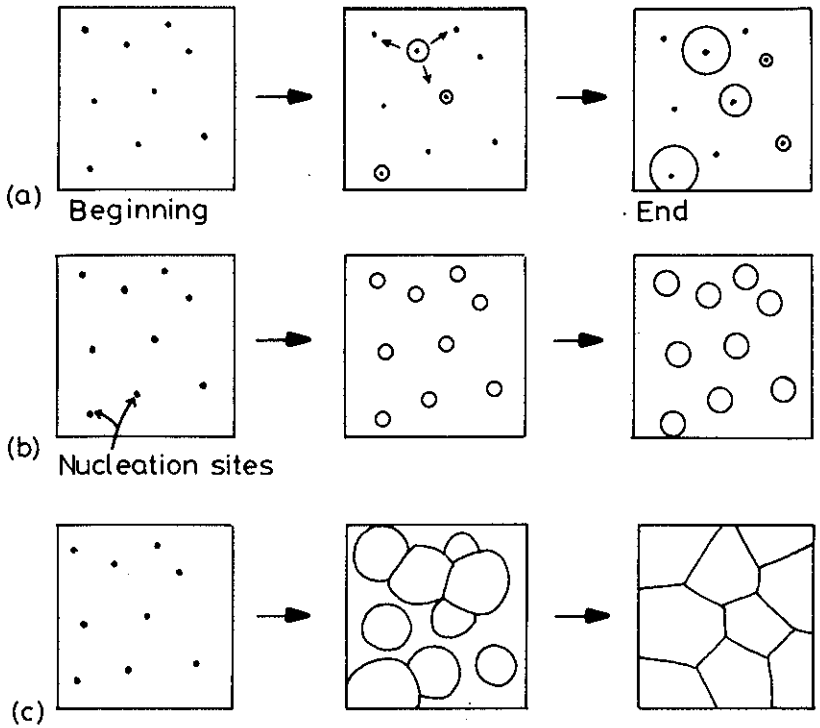

Fig. 5.24 (a) Nucleation at a constant rate during the whole transformation. (b) Site saturation—all nucleation occurs at the beginning of transformation. (c) A cellular transformation.

As a simple example of the derivation of $f(t, T)$ consider a cellular transformation ($\alpha \rightarrow \beta$) in which β cells are continuously nucleated throughout the transformation at a constant rate N[5]. If the cells grow as spheres at a constant rate v, the volume of a cell nucleated at time zero will be given by

$$V = \frac{4}{3}\pi r^3 = \frac{4}{3}\pi(vt)^3$$

A cell which does not nucleate until time τ will have a volume

$$V' = \frac{4}{3}\pi v^3(t - \tau)^3$$

The number of nuclei that formed in a time increment of $d\tau$ will be $N d\tau$ per unit volume of untransformed α. Thus if the particles do not impinge on one another, for a unit total volume

$$f = \Sigma V' = \frac{4}{3}\pi N v^3 \int_0^t (t - \tau)^3 \, d\tau$$

i.e.

$$f = \frac{\pi}{3} N v^3 t^4 \tag{5.37}$$

This equation will only be valid for $f \ll 1$. As time passes the β cells will eventually impinge on one another and the rate of transformation will decrease again. The equation valid for randomly distributed nuclei for both long and short times is[6]

$$f = 1 - \exp\left(-\frac{\pi}{3} N v^3 t^4\right) \tag{5.38}$$

Note that this is the same as Equation 5.37 for short times, since $1 - \exp(-z) \simeq z$ when $z \ll 1$. It is also reasonable for long times since as $t \to \infty, f \to 1$.

Equation 5.38 is known as a *Johnson–Mehl–Avrami equation*. In general, depending on the assumptions made regarding the nucleation and growth processes, a variety of similar equations can be obtained with the form

$$f = 1 - \exp(-kt^n) \tag{5.39}$$

where n is a numerical exponent whose value can vary from ~1 to 4. Provided there is no change in the nucleation mechanism, n is independent of temperature. k, on the other hand, depends on the nucleation and growth rates and is therefore very sensitive to temperature. For example, in the case above, $k = \pi N v^3/3$ and both N and v are very temperature sensitive.

Since $\exp(-0.7) = 0.5$ the time for 50% transformation ($t_{0.5}$) is given by

$$kt_{0.5}^n = 0.7$$

i.e.

$$t_{0.5} = \frac{0.7}{k^{1/n}} \tag{5.40}$$

For the case discussed above

$$t_{0.5} = \frac{0.9}{N^{1/4} v^{3/4}} \tag{5.41}$$

Consequently it can be seen that rapid transformations are associated with large values of k, i.e. rapid nucleation and growth rates, as expected.

Civilian transformations that occur on cooling are typified by C-shaped TTT curves as shown in Fig. 5.23a. This can be explained on the basis of the variation of nucleation and growth rates with increasing undercooling. At temperatures close to T_e the driving force for transformation is very small so that both nucleation and subsequent growth rates are slow and a long time is required for transformation. When ΔT is very large, on the other hand, slow diffusion rates limit the rate of transformation. A maximum rate is, therefore, obtained at intermediate temperatures.

5.5 Precipitation in Age-Hardening Alloys

The theory of nucleation and growth that has been described above is able to provide general guidelines for understanding civilian transformations. Let us now turn to a consideration of some examples of the great variety of civilian transformations that can occur in solids, and begin with alloys that can be age-hardened. These alloys are characterized by phase diagrams such as that shown in Fig. 5.1a(i). Two extensively researched and illustrative examples are aluminium-copper and aluminium-silver alloys.

5.5.1 Precipitation in Aluminium-Copper Alloys

GP Zones

Figure 5.25 shows the Al-rich end of the Al–Cu phase diagram. If an alloy with the composition Al–4 wt% Cu (1.7 atomic %) is heated to a temperature of about 540 °C all copper will be in solid solution as a stable fcc α phase, and by quenching the specimen rapidly into water there is no time for any transformation to occur so that the solid solution is retained largely unchanged to room temperature. However, the solid solution is now supersaturated with Cu and there is a driving force for precipitation of the equilibrium θ phase, $CuAl_2$.

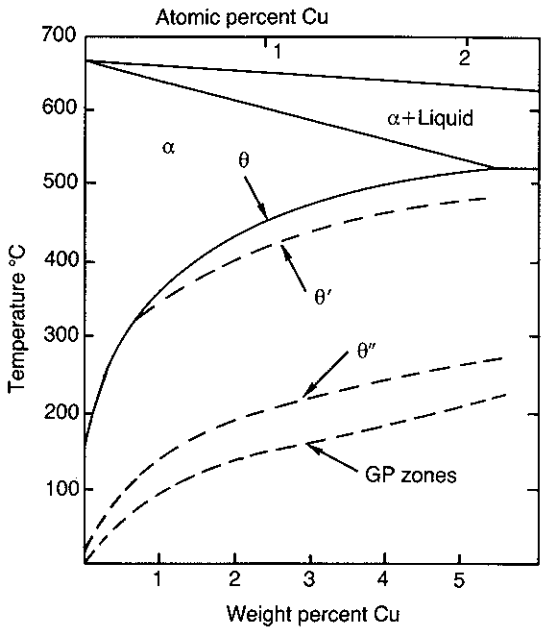

Fig. 5.25 Al–Cu phase diagram showing the metastable GP zone, θ″ and θ′ solvuses. (Reproduced from G. Lorimer, *Precipitation Processes in Solids*, K.C. Russell and H.I. Aaronson (Eds.), The Metallurgical Society of AMIE, 1978, p. 87.)